Journal of Cleaner Production 477 (2024) 143838

Contents lists available at ScienceDirect

Journal of Cleaner Production

journal homepage: www.elsevier.com/locate/jclepro

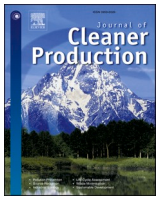

# Solar-driven calcination of clays for sustainable zeolite production: CO2 capture performance at ambient conditions

Pelin Pasabeyoglu [a,b], Erdem Deniz [c], Gkiokchan Moumin [d], Zafer Say [c,*], Burcu Akata [a,b,**]

[a] Micro and Nanotechnology Programme, Middle East Technical University, 06800, Ankara, Turkey
[b] Central Laboratory, Middle East Technical University, 06800, Ankara, Turkey
[c] Materials Science and Nanotechnology Engineering, TOBB University of Economics and Technology, 06510, Ankara, Turkey
[d] Institute of Future Fuels, German Aerospace Center (DLR), 51147, Cologne, Germany

ARTICLE INFO

Handling Editor: Panos Seferlis

*Keywords:*
Kaolin
Halloysite
Solar calcination
$CO_2$ capture
Green zeolite

ABSTRACT

This study presents the environmentally sustainable synthesis of zeolites from solar-calcined kaolin and halloysite, emphasizing their application in $CO_2$ capture due to their distinctive porous structures and chemical attributes. Expanding upon prior research that utilized solar energy for kaolin calcination, we now explore halloysite as an alternative clay mineral for zeolite production and $CO_2$ capture. Employing a solar simulator, halloysite was calcined at temperatures ranging from 700 to 1000 °C, resulting in the synthesis of zeolites 4A and 13X via hydrothermal methods. The synthesized zeolites were characterized using X-ray diffraction (XRD), low angle XRD (LA-XRD), transmission electron microscopy (TEM), and field-emission scanning electron microscopy (FE-SEM), and Brunauer–Emmett–Teller (BET) surface area measurements. Notably, the presence of Al-Si spinel, which crystallizes at elevated solar calcination temperatures, persisted within the zeolite 13X matrix, inducing a secondary mesoporous phase. The observed hysteresis in 13X samples, rather than confirming the mesoporous character of zeolite 13X, indicates a tandem effect of mesoporous Al-Si spinel with microporous zeolite 13X, exemplifying systems known as micro/mesoporous zeolitic composites (MZCs). The correlation obtained between the interplanar distances calculated from LA-XRD and pore size distributions acquired from the BJH desorption branches highlights LA-XRD as an alternative analysis method for assessing mesoporosity. While the microporosity of Al-Si spinel possessing 13X samples positively correlates with $CO_2$ capture performance, mesoporosity appears to have minimal impact. Among the zeolites synthesized using solar energy, zeolite 4A (LTA) demonstrates superior $CO_2$ capture capability, achieving an adsorption capacity of 2.15 mmol/g at 25 °C and 1 bar. This study highlights the potential of solar energy in producing eco-friendly zeolites from kaolin and halloysite for improved $CO_2$ capture, advancing sustainable environmental solutions.

## 1. Introduction

Kaolinite and halloysite, as clay minerals, have pivotal roles in diverse industries, including ceramics, chemicals, and food production as well as in the creation of geopolymers, geopolymer-based composites, zeolites, and intercalates (Bundy, 1993; Zhang et al., 2020; Buyondo et al., 2022). The transformations occurring during the thermal treatment of kaolin (clay which is rich in kaolinite mineral) and halloysite, and their mechanisms and kinetics, have been extensively investigated using various methods. During the calcination of kaolin and halloysite, distinct thermal processes occur at different temperature ranges. Dehydroxylation takes place at 450–700 °C, converting the clay into its reactive amorphous meta phase. The clay material goes through an Al-Si spinel crystallization at elevated temperatures of 925–1050 °C resulting in the simultaneous formation of amorphous silica (Ptáček et al., 2010). Upon calcination, these minerals transform into their respective meta-forms, exhibiting enhanced reactivity and porosity (Bakera and Alexander, 2019). This thermal alteration not only broadens their utility in the synthesis of advanced materials like zeolites but also highlights their significance in sectors demanding high-performance, environmentally sustainable materials (Novembre et al., 2011; Belviso et al., 2013; Kirdeciler and Akata, 2020). When the transition from raw to calcined states is achieved by solar calcination, it unlocks new potentials, paving the way for innovations in environmental remediation,

* Corresponding author.
** Corresponding author. Micro and Nanotechnology Programme, Middle East Technical University, 06800, Ankara, Turkey.
*E-mail addresses:* zsay@etu.edu.tr (Z. Say), akata@metu.edu.tr (B. Akata).

https://doi.org/10.1016/j.jclepro.2024.143838
Received 3 May 2024; Received in revised form 23 July 2024; Accepted 30 September 2024
Available online 1 October 2024
0959-6526/© 2024 Elsevier Ltd. All rights are reserved, including those for text and data mining, AI training, and similar technologies.

industrial processes, and green technology developments.

The urgent need to address global warming has driven the advancement of zeolites, crystalline hydrous aluminosilicates, as highly efficient and cost-effective porous adsorbents for $CO_2$ capture, leveraging their unique 3D frameworks and microporous nature (Sanz-Pérez et al., 2016). Their exceptional attributes, such as extensive surface area, high porosity, and adjustable acidity, render them vital in carbon dioxide capture technologies, especially in selectively adsorbing $CO_2$ from various gas streams, including flue gases and ambient air (Zhang et al., 2024). Zeolites' well-defined pore structure enables the selective adsorption of $CO_2$ molecules, crucial for effective carbon dioxide capture, while their surfaces can be modified to enhance $CO_2$ affinity through ion-exchange processes for improved interaction (Kumar et al., 2020). Importantly, zeolites sustain their structural integrity under the high temperatures often found in industrial gas streams, making them ideal for carbon capture and sequestration (CCS) applications (Boer et al., 2023). Their ability to be regenerated, allowing for repeated $CO_2$ adsorption and desorption cycles, underscores their economic feasibility for large-scale carbon management. Ongoing research is dedicated to refining zeolite structures for maximal $CO_2$ uptake, devising economical synthesis methods, and incorporating zeolite-based systems into existing industrial frameworks, with material science innovations continuously enhancing their $CO_2$ capture efficiency and selectivity. Before moving on to the efficiency and selectivity of the zeolites, cost-effective, green, and sustainable synthesis of zeolites should be addressed.

The escalating demand for zeolites, driven by their critical role in catalysis, gas separation, and $CO_2$ capture, necessitates the development of environmentally sustainable production methods. Traditional zeolite production techniques often rely on energy-intensive calcination of clays, which depend on nonrenewable resources and result in significant $CO_2$ emissions. In contrast, solar calcination as a novel approach offers a greener alternative, leveraging renewable solar energy to reduce the environmental footprint.

This study distinguishes itself from conventional zeolite 13X synthesis methods through several key innovations. Unlike traditional approaches that often rely on structure-directing agents (SDAs) and additional silica sources, our method eliminates the need for these extra components, simplifying the synthesis process and reducing associated costs and environmental impacts (Maschmeyer and van de Water, 2006; Martínez T. et al., 2019). A notable feature of our zeolite 13X samples is the mesoporosity induced by the presence of Al-Si spinel, formed during high-temperature solar calcination. This approach contrasts with the traditional methods of inducing mesoporosity through organic templates or post-treatments (Groen et al., 2004; Chen and Ahn, 2014; Qoniah et al., 2015; Sachse et al., 2017; Panda et al., 2020). Furthermore, our approach utilizes solar-calcined clay as the precursor, as opposed to the ultra-pure, expensive chemicals typically used in zeolite synthesis. The use of solar energy presented in this work not only provides a sustainable and eco-friendly alternative to fossil fuel-based calcination but also underscores the practicality and cost-effectiveness of our method. These innovations collectively enhance the performance and sustainability of the synthesized zeolites, particularly in applications such as $CO_2$ capture.

In a recent study published by our research group, solar energy was demonstrated for metakaolin production at high temperatures, a viable precursor for synthesizing zeolites 4A and 13X (Pasabeyoglu et al., 2023). This novel approach, leveraging a solar-heated rotary kiln, enabled the transformation of kaolin at temperatures between 700 and 1000 °C. Our findings reveal that metakaolin obtained through solar calcination facilitates the synthesis of high-quality zeolites, demonstrating a sustainable and energy-efficient alternative to conventional methods reliant on fossil fuels.

Building on previous research that pioneered the use of solar energy for kaolin calcination, we extend our investigation to halloysite, exploring its potential as an alternative feedstock for zeolite production and $CO_2$ capture. Halloysite was subjected to solar calcination using a solar simulator, with temperatures ranging from 700 to 1000 °C, to achieve the necessary dehydroxylation process for transforming halloysite into a reactive meta phase. The solar calcined halloysite was then utilized as a precursor for synthesizing zeolites 4A and 13X through optimized hydrothermal methods without any addition of extra silica source or structure directing agents (SDA). The synthesized zeolites underwent rigorous characterization using X-ray diffraction (XRD) and low-angle XRD (LA-XRD) for phase identification, transmission electron microscopy (TEM), and field-emission scanning electron microscopy (FE-SEM) for morphological analysis, and Brunauer–Emmett–Teller (BET) surface area measurements to assess porosity. Additionally, the $CO_2$ adsorption capacity of the synthesized zeolites was evaluated at ambient conditions (25 °C and 1 bar) to determine their suitability for carbon capture applications.

The results not only confirm that solar-calcined halloysite is an effective precursor for zeolite synthesis comparable to kaolin but also highlight the $CO_2$ capture capability of these solar-produced zeolites, contributing to the broader objective of sustainable and eco-friendly zeolite synthesis and application. In addition, the presence of Al-Si spinel within the zeolite 13X matrix, resulting from high-temperature solar calcination, introduces a secondary mesoporous phase that can potentially enhance the material's adsorption properties. This work emphasizes the potential of solar calcination as a viable and environmentally conscious route for the mass production of mineral-derived precursors for value-added products, with implications for both zeolite synthesis and $CO_2$ capture technologies.

## 2. Materials and methods

### 2.1. Materials and synthesis

The clay samples halloysite and kaolin used for solar calcination were obtained commercially from Turkey. The chemical compositions of halloysite (H) and kaolin (K) were analyzed using Rigaku ZSX Primus II X-ray fluorescence spectrometer (XRF). Halloysite and kaolin primarily consist of silicon dioxide (H: 44.0 wt%, K: 46.1 wt%) and alumina (H: 39.4 wt%, K: 38.3 wt%). The Si/Al molar ratios of halloysite and kaolin were calculated to be 0.95 and 1.02, respectively.

Solar calcined (SC) clays were obtained using a solar simulator and a rotary kiln located in Deutsches Zentrum für Luft-und Raumfahrt (DLR), Cologne, Germany. Details of the solar simulator calcinations can be found in previous work (Pasabeyoglu et al., 2023). The rotary kiln (3 rpm) was loaded with 1 kg of halloysite and heated using lamps with a maximum power input of 5.6 kW. The temperature was controlled using thermocouples, and the power was adjusted to either reduce or maintain the temperature for 2 h. Afterward, the lamps were turned off, and the material was removed once it cooled. SC samples were named HSC for halloysite and KSC for kaolin followed by average bed temperature (avgT).

SC clays were used as both $SiO_2$ and $Al_2O_3$ sources and the zeolite gel formula used in synthesis from HSC was $2.04SiO_2$:$1Al_2O_3$:$3.14Na_2O$:$110H_2O$ following a standard hydrothermal synthesis (Pasabeyoglu et al., 2023). Sigma Aldrich Chemicals provided the sodium hydroxide (NaOH) pellets. Deionized water (DDW) was obtained by distilling running tap water using a water purification system (Milli-Q system, $\leq$18 Ω). The predetermined quantities of NaOH (2.53 g) and DDW (19.76 g) were combined with HSC (2.70 g) to create a gel in a 30 ml high-density polyethylene (HDPE) bottle. The gel was then aged for 4 h in a water bath at 60 °C with continuous agitation. This was followed by 4 h of static reaction in a preheated oven at 100 °C. The resulting solid particles were centrifuged, washed, and dried overnight. Zeolite samples were denoted Z-HSC-avgT and Z-KSC-avgT for halloysite and kaolin, respectively.

### 2.2. Characterization methods

Powder X-ray diffraction (PXRD) patterns were determined by a Rigaku Miniflex instrument operating at 40 kV and 15 mA. Low-angle XRD measurements were acquired with Rigaku Ultima IV operating at 40 kV and 30 mA with Parallel Beam geometry, adjusted slits, and CuKα radiation. The morphology of the samples was characterized by the scanning electron microscopy (SEM) using a FEI Quanta 400 instrument equipped with an energy-dispersive X-ray spectroscopy (EDX). Transmission electron microscopy (TEM) analysis was performed with a JEOL JEM-2100F operated at 200 kV. Samples were suspended and sonicated in ethanol for 5 min, then dropped on a carbon film-covered copper grid. Nitrogen adsorption–desorption isotherms, surface area, pore size distribution, and pore volume were determined through nitrogen adsorption–desorption measurements at −196 °C using a Quantachrome Autosorb 1-C instrument. Prior to measurements, the samples were outgassed in vacuum at 250 °C for 8 h. The total surface area was calculated using the BET method. The pore size distribution in the mesopore range was analyzed using the Barrett–Joyner–Halenda (BJH) model based on the desorption branch of isotherms. Mesopore volume was calculated by subtracting the micropore volume (calculated by the t-plot method) from the total pore volume, which was determined from the amount of $N_2$ adsorbed at $P/P_0 = 0.99$. All characterizations of raw materials and final products were conducted at the Middle East Technical University (METU) Central Laboratory in Turkey.

### 2.3. $CO_2$ capture measurements

The compact and fully automated catalyst characterization system, CatLab-2, developed by Specson Instruments (specsoninstruments.com), was utilized to conduct $CO_2$ capture measurements, as depicted in Fig. 1.

This system is equipped with five Bronkhorst Mass Flow Controllers (MFCs) and a fixed-bed quartz tubular reactor measuring 220x10 × 8 mm, which is connected to an SRS RGA 200 mass spectrometer for the capability of analyzing gases in real-time. Additionally, the system features an integrated furnace capable of reaching temperatures up to 900 °C, facilitating high-temperature pre-treatments to eliminate water from the porous structures.

In a standard procedure for capturing $CO_2$, 300 mg of the sorbent is placed inside a quartz reactor. Before proceeding with the adsorption tests, each sorbent sample undergoes a thermal activation process. This involves heating the sample to 350 °C with an argon flow of 100 standard cubic centimeters per minute (sccm) for 2 h. Following this, the sample is cooled to ambient temperature and allowed to stabilize under a continuous argon flow for an additional 60 min. This outgassing phase is essential for eliminating previously adsorbed gases and moisture within the sorbent's pores. Subsequently, a mixture containing 2% $CO_2$ in argon gas is introduced into the reactor at a flow rate of 20 sccm, maintaining room temperature and a pressure of 1 bar for 3 h. Throughout this experiment, the mass spectrometer continuously tracks the m/z 44 signal, providing real-time data for the dynamic breakthrough curves, as illustrated in Fig. 2.

To calculate total $CO_2$ capture capacity in mmol/g, we routinely perform blank experiments with the same recipe without including the sorbent material. These blank tests are crucial for accounting for any inherent delays in the breakthrough curves that might arise from the design of the reactor or the length of the tubing extending from the Mass Flow Controllers (MFCs) to the mass spectrometer, effectively removing

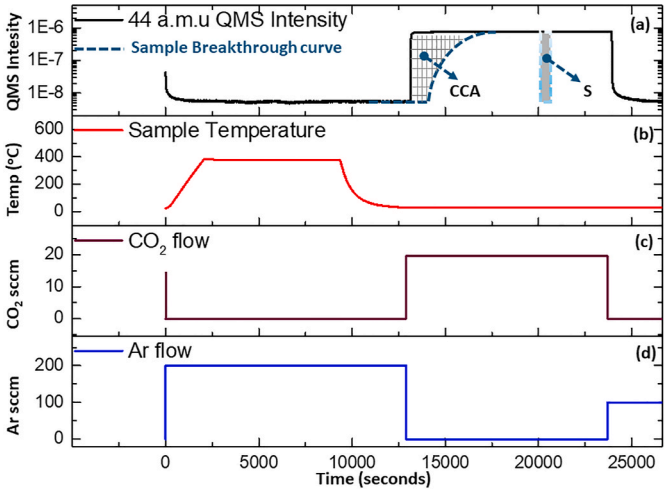


**Fig. 2.** Experimental outputs of each parameter during typical $CO_2$ capture analysis. (a) $CO_2$ breakthrough curve based on QMS intensity of 44 a.m.u signal, (b) temperature reading from K-type thermocouple standing just 5 mm above the sorbent material, (c) and (d) $CO_2$ and Ar gas flow in sccm during the analysis. CCA refers to the $CO_2$ Capture Area and S refers to the calibration.

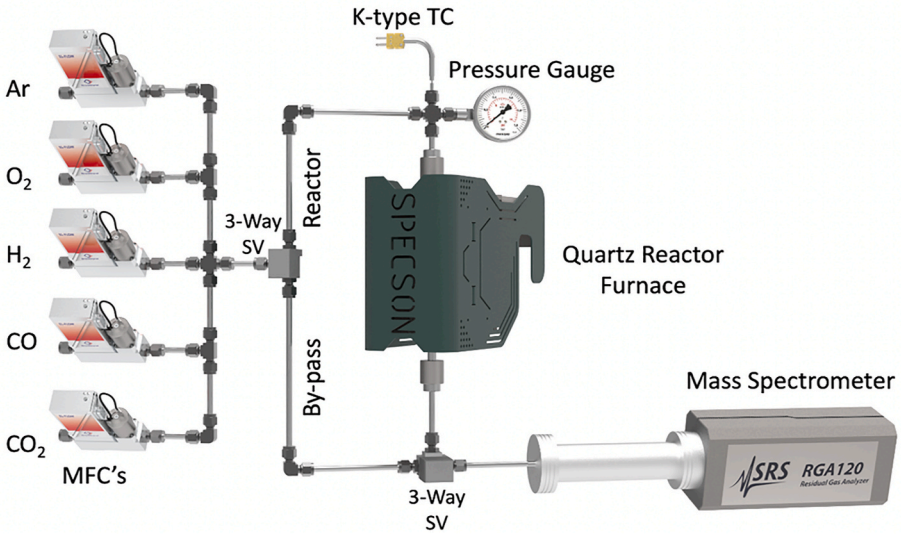


**Fig. 1.** Schematic of the analysis unit. 5 different gases can be mixed at a certain ratio and fed into reactor at constant flow or directly by-passed to analyzer for calibration by switching 3-Way valves. Reactor furnace can be set up to 900 °C and the temperature is monitored by K-type thermocouple. Outlet gas mixture is analyzed in real-time by residual gas analyzer.

background influences. The $CO_2$ capture calculation is based on the integration of calibrated area (S) generated by a certain concentration of $CO_2$ (2% diluted in Ar) gas at constant 20 sccm flow. Calibrated area (S) refers to the amount of total $CO_2$ gas flowing for a certain period of time (i.e. 10 min) and can be calculated by equation (1):

$$S = \frac{(0.987 atm \times V_{total})}{(0.082057\ L \times atm \times mol^{-1} \times K^{-1}) \times 298.15K} \quad (1)$$

where $V_{total}$ is:

$$V_{total} = 10\ \text{min} \times 20\ \frac{cm^3}{min} CO_2\ in\ Ar \times \frac{2}{100}$$

S value is used as a reference for the calculation of total $CO_2$ quantity based on $CO_2$ capture area (CCA) value specific for each sorbent material. Captured $CO_2$ quantity can be calculated by equation (2):

$$Captured\ CO_2\ Quantity = CCA \div S \times \frac{1g}{300\ mg} \quad (2)$$

## 3. Results and discussions

### 3.1. Characterization of the halloysite and metahalloysites

The XRD pattern of the halloysite used in this study is depicted in Fig. 3a. The halloysite was characterized by prominent peaks at 11.9° (2θ), 19.94° (2θ), and 24.42° (2θ), corresponding to d-spacings of 7.4, 4.5, and 3.6 Å, respectively, and representing the (001), (100), and (002) reflection planes (Card # 00-029-1487). The presence of a diffraction peak at 11.9°, corresponding to a 7.4 Å interplanar distance (d), confirms the mineral as halloysite-7 Å. In addition to the halloysite peaks, the XRD pattern also exhibited reflection peaks of quartz (Card # 01-089-8937) as an impurity. Quantitative analysis of the halloysite sample indicated a composition of >90 wt% halloysite.

The microphotograph captured by the field emission scanning electron microscopy (FE-SEM) (Fig. 3b) shows that the halloysite exhibited a tubular shape and a one-dimensional (1-D) hollow tube structure with consistent diameter. The tube diameters generally varied between approximately 40 to 100 nm, with the lengths averaging between 0.2 and 0.5 μm. The FE-SEM-EDX (Field Emission Scanning Electron Microscopy with Energy-Dispersive X-ray Spectroscopy) analysis conducted on halloysite sample was depicted in the same figure. From this data, the Si/Al was calculated to be 0.94, which corroborates closely with the ratio of 0.95 obtained from X-ray fluorescence (XRF) spectroscopy. This consistency in Si/Al ratios from independent analytical methods substantiates the reliability of the elemental composition findings for the halloysite samples under study.

The XRD patterns of metahalloysites show a diffuse halo pattern indicative of amorphous metahalloysite, composed of free silica interspersed with alumina or silica-alumina phases (Fig. 4a) (Chakraborty et al., 2003). Calcined halloysites were fully transformed into metahalloysites, as evidenced by the lack of halloysite peaks. Quartz peaks were present in all patterns. At 870 °C, nanocrystallites of Al-Si spinel (gamma-alumina type) began to form, indicated by peaks at 37.4°, 45.90°, and 66.94° (Fig. 4b). These peaks correspond to the (311), (400), and (440) planes of gamma alumina, respectively, with a Halder-Wagner crystallite size of 4.4 nm (Urbonavicius et al., 2020). The formation of Al-Si spinel occurs in the temperature range of 925 °C–1050 °C, accompanied by the generation of amorphous silica, potentially increasing the Si/Al ratio in metahalloysite (Ptáček et al., 2010, 2013; Yuan et al., 2012; Chauffeton and Wallez, 2022). As metahalloysite breaks down at high temperatures, the resulting crystalline Al-Si spinel would reduce the accessible alumina content. Simultaneously, liberated amorphous silica might serve as a silica source during zeolite synthesis nucleation.

### 3.2. Characterization of the zeolites

Fig. 5 showcases the crystal morphology of the synthesized zeolites. The FE-SEM images for zeolites synthesized from halloysite calcined at

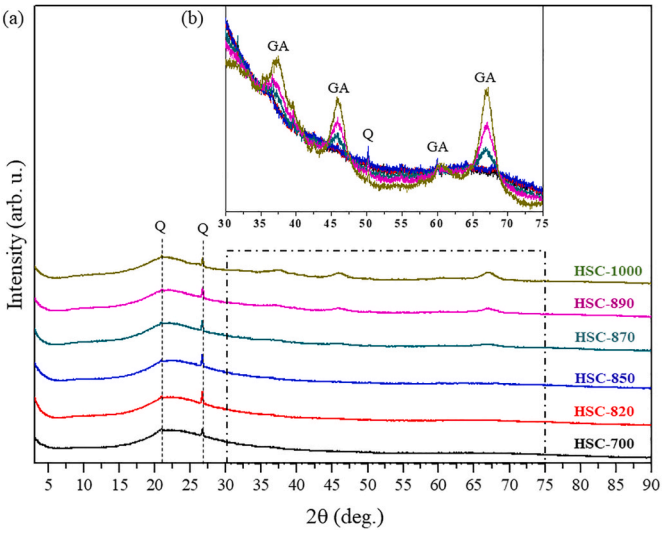


**Fig. 4.** (a) XRD patterns of metahalloysites and (b) an enlarged view highlighting the formation of Al–Si spinel (GA: gamma alumina (Al-Si spinel), Q: Quartz).

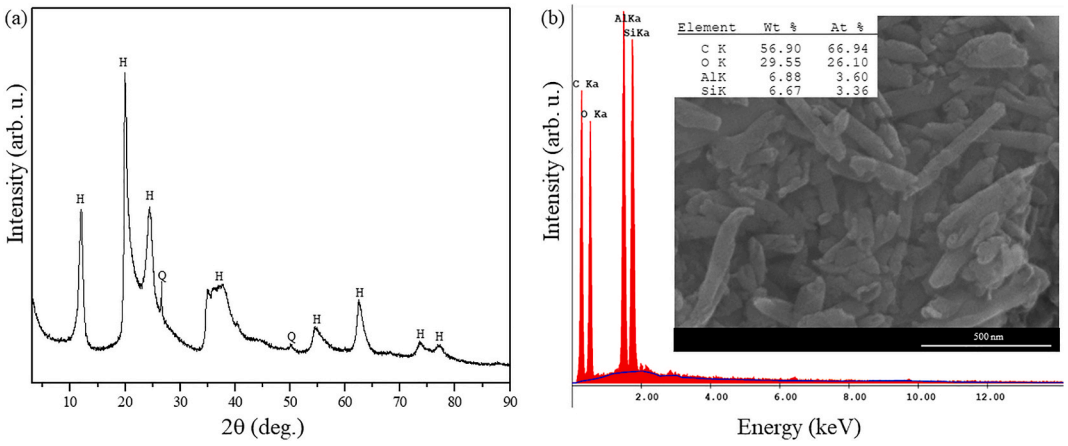


**Fig. 3.** (a) XRD pattern of halloysite and b) Scanning electron micrograph and EDX analysis of the halloysite (H: Halloysite, Q: Quartz).

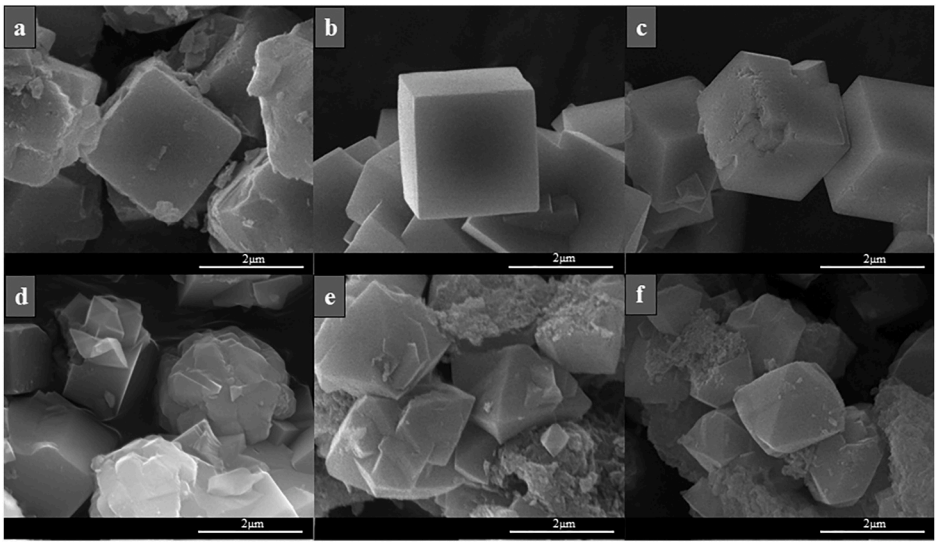


**Fig. 5.** SEM images of (a) Z-HSC-700, (b) Z-HSC-820, (c) Z-HSC-850, (d) Z-HSC-870, (e) Z-HSC-890, (f) Z-HSC-1000.

700 °C, 820 °C, and 850 °C (Fig. 5a, b, c) illustrate the development of cubic crystals with smooth exteriors, each measuring roughly 2 μm across, displaying features typical of the LTA (Linde Type A) structure. For the sample labeled Z-HSC-870 (Fig. 5d), there was an evident presence of a combination of zeolite types 4A and 13X, corroborating the findings from XRD analysis. The cubic crystals of zeolite 4A appeared to be exfoliated, which may account for the reduced crystallinity percentage deduced from the XRD results. Furthermore, the SEM images for the Z-HSC-890 and 1000 samples (Fig. 5e and f) reveal the octahedral crystalline form of zeolite 13X. The estimated particle size of the product is approximately 2 μm, with the formed zeolite crystals aggregating into conglomerates.

Fig. 6a displays the XRD patterns of the zeolite products synthesized from halloysite calcined using solar energy. The products obtained from halloysite calcined at 700 °C, 820 °C, and 850 °C yielded high-quality zeolite 4A products (Card # 04-009-4857) with a crystallinity exceeding 98%. Quartz was the only impurity, quantified at <5 wt%. The analysis revealed that zeolites synthesized from samples that were in meta forms exhibited nearly uniform quality, indicating that high-quality zeolite 4A can be effectively synthesized from metahalloysites produced across a broad spectrum of calcination temperatures when utilizing solar reactors. With the solar calcination temperature reaching 870 °C, a blend of zeolite 4A and zeolite 13X (Card # 00-038-0240) was produced. Notably, an increment in the calcination temperature led to a predominant formation of zeolite 13X, virtually eliminating the presence of zeolite 4A.

Fig. 6b illustrates that the blend sample Z-HSC-870 lacked any discernible diffraction patterns attributable to Al-Si spinel, in contrast to the samples Z-HSC-890 and Z-HSC-1000, which are composed purely of zeolite 13X and exhibit a pronounced spinel structure. Notably, the intensity of the spinel features escalated with increasing calcination temperature, implying the incorporation of spinel structures within the 13X zeolite matrices. Fig. 7 conducts a comparative analysis between the solar-calcined halloysite precursors and their resultant zeolite synthesis products. This comparison shows that the spinel content within the precursor of the blend sample HSC-870 was likely consumed during the zeolite synthesis process, as evidenced by the absence of spinel structure peaks in the synthesized material. Conversely, in the diffraction pattern of Z-HSC-890, the (400) plane of the spinel was distinctly observable, though with diminished visibility of other crystallographic planes, whereas in Z-HSC-1000, all characteristic peaks of the spinel structure were preserved, highlighting the differential impact of calcination temperature on the spinel phase retention within the synthesized zeolites.

Reflecting on the synthesis using solar-calcined kaolin, both studies indicate that high-quality zeolite 4A can be produced across a broad

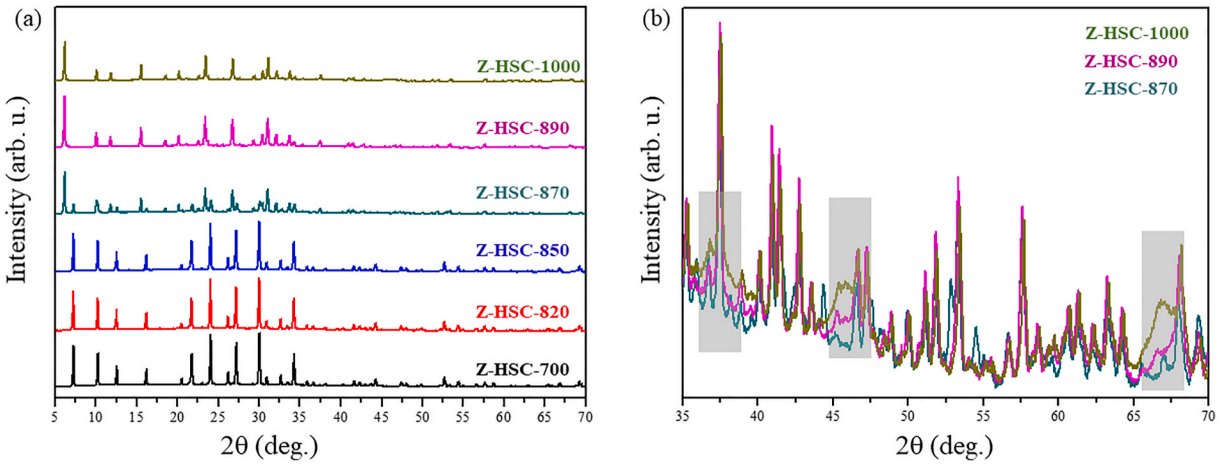


**Fig. 6.** (a) XRD patterns of the synthesized zeolites and (b) an enlarged view highlighting the presence of Al-Si spinel (GA: gamma alumina (Al-Si spinel)) in the zeolites.

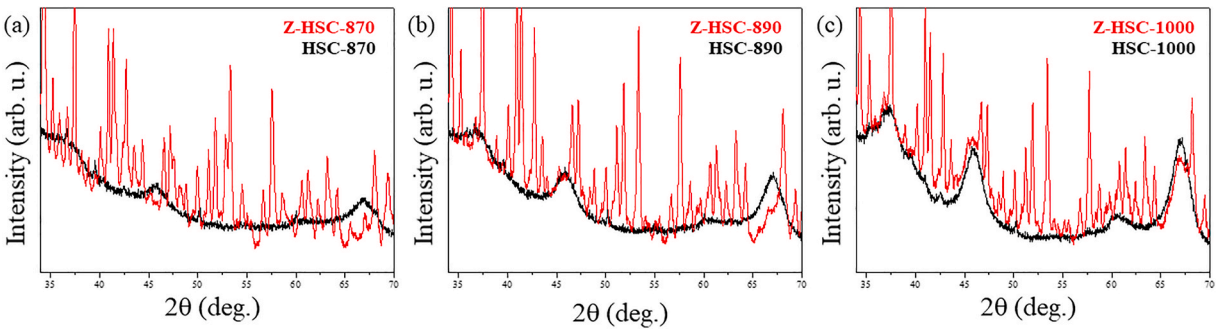


**Fig. 7.** XRD patterns of the precursor metahalloysites and the synthesized zeolites from them at calcination temperatures (a) 870 °C, (b) 890 °C, (c) 1000 °C to show Al-Si spinel presence in the zeolites.

range of calcination temperatures using solar reactors. The halloysite-derived zeolites tend to have slightly higher crystallinity percentages compared to those derived from kaolin. An increase in calcination temperature leads to a transition from zeolite 4A to 13X in both cases, though the specific temperatures at which these transitions occur differ slightly. The findings imply that both kaolin and halloysite can be effective precursor materials for synthesizing high-quality zeolites using solar calcination, with specific temperature thresholds guiding the resultant zeolite type and quality.

To investigate the occurrence and distribution of spinel within zeolite 13X, TEM images of the Z-HSC-890 sample are presented in Fig. 8. The TEM image (Fig. 8a) displayed zeolite 13X crystals predominantly exhibiting a well-defined octahedral morphology, confirming the SEM images, indicative of their crystalline nature. The edges of the crystals appear sharp, with smooth faces, suggesting a high degree of crystallinity. Adjacent to the zeolite crystals, there were patches of material with a contrasting appearance, indicating the presence of a secondary phase such as spinel (Fig. 8b). These inclusions were distinguishable by their different sizes, appearing as agglomerated nanoclusters, which have different orientations as fringes visible in high magnification (Fig. 8c). Accompanying SAED (Selected Area Electron Diffraction) pattern (Fig. 8d) revealed diffused rings arranged in a specific geometric pattern, confirming the nanocrystalline nature of the spinel.

The effect of Al-Si spinel was also observed in the textural characteristics of the zeolites. Fig. 9 shows the $N_2$ adsorption-desorption isotherms of the synthesized zeolites. It's important to acknowledge that the presence of $Na^+$ cations within the unit cell of zeolite LTA is known to restrict access to the zeolite's micropores for $N_2$ molecules (Cho et al., 2009). Consequently, when assessing zeolite 4A using $N_2$ physisorption, one can anticipate finding markedly low values for both the specific surface area and micropore volume (Palomino et al., 2010). Therefore, the $N_2$ adsorption-desorption isotherms for the samples Z-HSC-820, Z-KSC-740, Z-KSC-800, and Z-KSC-860, which consisted solely of pure zeolite 4A, were presented purely for illustrative purposes. All the other samples exhibited a very sharp initial rise in the quantity of $N_2$ adsorbed at relative pressures below 0.05 $P/P_0$, indicative of micropore filling. Blend samples Z-HSC-870 and Z-KSC-940 exhibited characteristic Type I (b) isotherm which was observed in materials that feature a wider range of pore sizes, encompassing larger micropores and potentially small mesopores (less than approximately 2.5 nm) (Thommes et al., 2015). Z-HSC-890 sample which had small amount of Al-Si spinel deviated from Type I(b) isotherm at high pressure range with a hysteresis. This type of hysteresis is called H4, and the adsorption branch now represents a combination of Types I and II isotherms, with the significant absorption at low relative pressures ($P/P_0$) linked to micropore filling. H4 hysteresis loops are commonly observed in materials such as aggregated zeolite crystals, certain mesoporous zeolites, and micro-mesoporous carbon structures (Thommes et al., 2015). As the Al-Si spinel crystallization became dominant in samples Z-HSC-1000 and Z-K-960, the type of isotherms turned into Type IV(a) isotherm in which capillary condensation was accompanied by some type of H3 hysteresis. In a recent study, empanada shape hysteresis obtained for some amorphous aluminosilicates was catalogued as H3(b), similar to samples as mentioned earlier showing an inflection point $P/P_0 \sim 0.87$ and closure at $P/P_0 \sim 0.5$ (Baldovino-Medrano et al., 2023). The proposed hysteresis type is effectively applicable to the Z-HSC-1000 and Z-K-960 samples, demonstrating that the nanocrystalline Al-Si spinel is the cause of the hysteresis observed. It's important to recognize that the observed hysteresis in 13X samples does not confirm the presence of mesoporous zeolite 13X; rather, it suggests a combined influence of the nanocrystalline mesoporous Al-Si spinel and microporous zeolite 13X, as identified through TEM analysis. This type of system where zeolite crystals are supported on a material that is typically mesoporous is known as micro/-mesoporous zeolitic composites (MZCs) or in short, zeolite composites (Pérez-Ramírez et al., 2008; Vu et al., 2016; Singh et al., 2021).

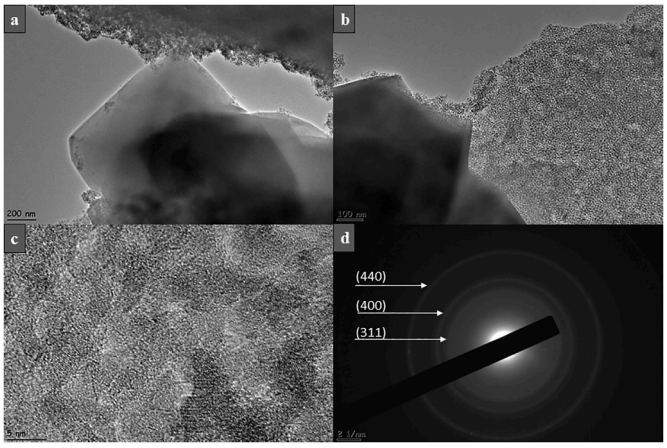


**Fig. 8.** TEM images of (a) and (b) Z-HSC-890 sample consisted of zeolite 13× and Al-Si spinel, (c) high magnification TEM image of Al-Si spinel fringes, and (d) selected area diffraction (SAED) recorded from (c).

Table 1 presents the textural properties of zeolites derived from solar-calcined kaolin and halloysite. It was observed that with increasing crystallinity in 13X zeolites, the mesopore volume decreased, resulting in microporosity percentages of 68%, 71%, and 87.5% for Z-KSC-960, Z-HSC-1000, and Z-HSC-890 samples, respectively. The multipoint BET surface areas of these 13X zeolites were consistent with existing literature values. The control sample, Z-KSC-980, which contained no zeolites but only Al-Si spinel and quartz, exhibited no microporosity, a low surface area, and predominantly mesopores.

Pore diameters derived from the BJH method's desorption branches and interplanar distances from low-angle XRD (LA-XRD) were compared in Fig. 10. LA-XRD has long been recognized as a rapid, non-destructive technique for assessing mesoporosity and pore size distribution in

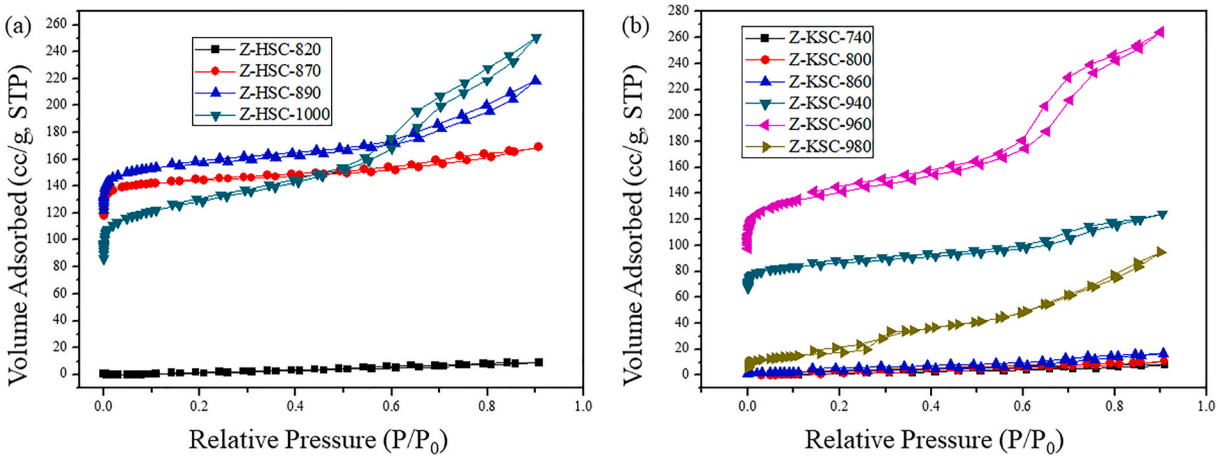


**Fig. 9.** The $N_2$ adsorption-desorption isotherms of (a) Z-HSC samples and (b) Z-KSC samples.

**Table 1**
Textural properties of synthesized zeolites.

| Sample | $S_{Total}$ ($m^2$/g)[a] | $S_{Ext}$ ($m^2$/g)[b] | $S_{Micro}$ ($m^2$/g)[b] | $V_{Total}$ (cc/g) | $V_{Meso}$ (cc/g)[c] | $V_{Micro}$ (cc/g)[b] | Microporosity (%) | XRD phases and zeolite crystallinity % |
|---|---|---|---|---|---|---|---|---|
| Z-KSC-940 | 327 | 58 | 269 | 0.13 | 0.02 | 0.11 | 85 | 4A, 56.6<br>13X, 62.4 |
| Z-HSC-870 | 555 | 38 | 517 | 0.22 | 0.01 | 0.21 | 95 | 4A, 45.3<br>13X, 69.6 |
| Z-KSC-960 | 527 | 153 | 374 | 0.22 | 0.07 | 0.15 | 68 | 13X, 91.4 |
| Z-HSC-1000 | 476 | 174 | 302 | 0.17 | 0.05 | 0.12 | 71 | 13X, 93.9 |
| Z-HSC-890 | 596 | 71 | 525 | 0.24 | 0.03 | 0.21 | 87.5 | 13X, 96.2 |
| Z-KSC-980 | 65 | 65 | – | 0.26 | 0.26 | – | 0 | Al-Si spinel and quartz |

[a] Multipoint BET.
[b] t-Method.
[c] Estimated by subtracting Vmicro from total pore volume.

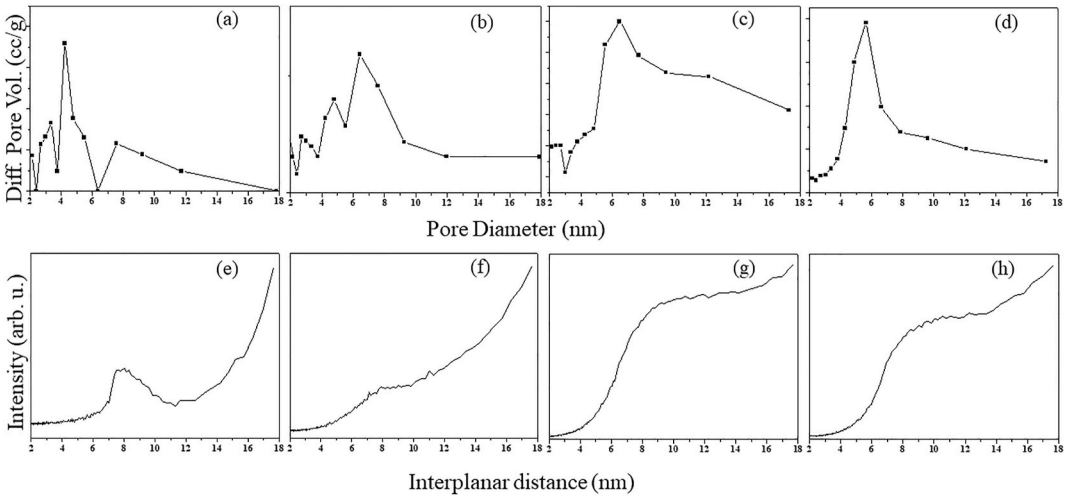


**Fig. 10.** Barrett–Joyner–Halenda (BJH) pore size distributions (PSD) and interplanar distances from low-angle XRD (LA-XRD) of (a) (e) Z-HSC-820, (b) (f) Z-HSC-870, (c) (g) Z-HSC-890, (d) (h) Z-HSC-1000, respectively.

zeolitic materials, complementing traditional methods (Fenelonov et al., 1999; Ishii et al., 2013; Sachse et al., 2017; Yassin et al., 2021). It was worth noticing that these two methods were complementary to each other on the zeolites' pore size estimations in our study. Given in Fig. 10a and d, Z-HSC-820 zeolite 4A sample showed a pore size distribution in the range of 6–11 nm, even though the zeolite 4A was known to be microporous. This phenomenon can be explained by the intercrystalline mesoporosity, often introduced during the course of crystallization generally generated by the aggregation of zeolite nanocrystals (Xue et al., 2012; Feng et al., 2013; Li et al., 2015; Hartmann

et al., 2021; Indira and Abhitha, 2022).

In the Z-HSC-870 blend, where the spinel structure was nearly absent, the pore size distribution (PSD) exhibited a minor peak at 6–9 nm (Fig. 10b–f). This minor peak indicates the presence of small mesopores. Conversely, the emergence of Al-Si spinel was marked by a distinct rise in the PSD curve from 5 nm onwards, as observed in both Z-HSC-890 and Z-HSC-1000 samples (Fig. 10c–g, d, h). This rise covers a broad range of pore sizes, suggesting that the formation of Al-Si spinel contributes to the development of a more diverse mesoporous structure. Notably, in the Z-HSC-1000 sample, the PSD was narrower and more defined compared to Z-HSC-890, reflecting a more uniform pore size distribution. The non-local density functional theory (NLDFT) pore size distribution model was also applied to the Z-HSC-890 and Z-HSC-1000 samples, as shown in SI-1 and SI-2, respectively. Although NLDFT provides a more detailed analysis of micro-mesoporous structures, the mesopore size distribution derived from the BJH desorption branch remains the standard for zeolites (Ojeda et al., 2003; Chen and Ahn, 2014; Lixia Bao, Peifeng Gao, 2020). In this study, both methods yielded consistent results for the synthesized samples.

Similar observations were made for the Z-KSC samples. For the Z-KSC-800 sample, which primarily consisted of zeolite 4A, a d-spacing of 13 nm indicated intercrystalline mesoporosity, although this was not prominently reflected in the PSD (Fig. 11a and b). As calcination temperatures increased, the Z-KSC-940 sample began to show a PSD that aligns with both Fig. 11a and b, indicating the development of mesopores. The Z-KSC-960 sample, identified as zeolite 13X, exhibited a broad PSD distribution in Fig. 10a. However, the pore diameter derived from the BJH method's desorption branch showed a narrower distribution, with a dominant pore size of 6 nm, suggesting a more uniform mesoporous structure.

### 3.3. $CO_2$ adsorption performance

The breakthrough curves based on dynamic CO2 adsorption on ten kaolin and halloysite-based zeolite samples are shown in Fig. 12. These curves were recorded under exposure to a 2% $CO_2$ in Ar mixture at ambient conditions. The red dashed line, intercepting the time axis at the 13,080th second, represents the gas switch point from only Ar to the 2% $CO_2$ mixture. The red circles on each curve indicate the points where the first $CO_2$ signal was detected by the QMS. The time interval between the dashed line and the red circle, during which no $CO_2$ signal is detected, demonstrates the filling of the available pore volume of each porous sorbent material. This interval reflects the $CO_2$ adsorption capacity and efficiency of the different zeolite samples.

The comparative analysis of the breakthrough curves was used to give insights into the dynamics of $CO_2$ adsorption on these materials. For the 4A zeolite samples represented in Fig. 12a, a long delay between the gas switch (red dashed line) and the onset (red circle) may suggest a large micropore volume and/or a more effective adsorption affinity. The interval before $CO_2$ was detected following its introduction to the zeolite serves as an indicator of how readily the $CO_2$ molecules enter and are taken up by the zeolite's pores. A longer delay suggests that the $CO_2$ is interacting with and being adsorbed by the zeolite's internal structure rather than merely occupying the space at the pore entrances. This delay can be attributed to a larger pore volume, which allows more $CO_2$ to be adsorbed before it becomes detectable by the QMS, and a stronger adsorption affinity, whereby $CO_2$ molecules are more effectively captured by the zeolite's active sites. Furthermore, the rate of $CO_2$ diffusion into the zeolite is a key factor; a longer delay may indicate slower diffusion. While slower diffusion might seem less efficient, it can signal that more extensive adsorption is taking place within the material's structure, suggesting that the $CO_2$ is being thoroughly incorporated into the zeolite, and not just on its surface. The slope of the breakthrough curves following the initial $CO_2$ detection provides insight into the rate at which the zeolite approaches its maximum adsorption capacity. A gradual increase hints at a controlled rate of $CO_2$ adsorption, likely due to the zeolite having a significant pore volume that requires a longer duration to reach full $CO_2$ saturation. Observing this less steep trajectory in the curves of 4A zeolite samples implies a moderated adsorption rate, a characteristic that could be strategically advantageous for prolonged and steady $CO_2$ sequestration, ensuring consistent capture over an extended period. Saturation is reached when the curve levels off, indicating that no further increase in $CO_2$ is detected, and the zeolite is fully saturated with $CO_2$. A longer time to reach this saturation plateau suggests a larger adsorption capacity. Generally, the 4A zeolite samples exhibit a faster response to $CO_2$ adsorption, while the blend (Z-HSC-870, Z-KSC-940) and 13X samples (Z-HSC-890, Z-HSC-1000, Z-KSC-960) in Fig. 12b have a more gradual adsorption process, likely due to their different pore structures and compositions.

The examination of $CO_2$ adsorption efficiency across different zeolite types reveals a clear distinction in performance based on structural characteristics, as demonstrated in Fig. 13. Starting with the 4A zeolites, their higher $CO_2$ capture capacity stands out as a significant feature. This capacity is largely attributed to their uniform microporous structure, which facilitates dense packing and efficient utilization of adsorption sites. The 4A zeolites' inherent crystalline framework, occupied with $Na^+$ sites, creates an environment for strong electrostatic interactions with $CO_2$ molecules, thus optimizing $CO_2$ uptake (Indira and Abhitha, 2022). The 4A samples show a remarkable capability to adsorb more $CO_2$ per gram than the other zeolites tested, reaching the highest value of 2.15 mmol/g. Z-KSC-960 and Z-HSC-1000, which have microporosity percentages of 68% and 71%, respectively, demonstrate a trend where a lower percentage of microporosity corresponds to a reduced $CO_2$ capture capacity. This is likely due to the fewer micropores available for $CO_2$ to adsorb onto, resulting in quicker saturation and a reduced overall capacity for $CO_2$ capture. In contrast, Z-HSC-890, with a higher

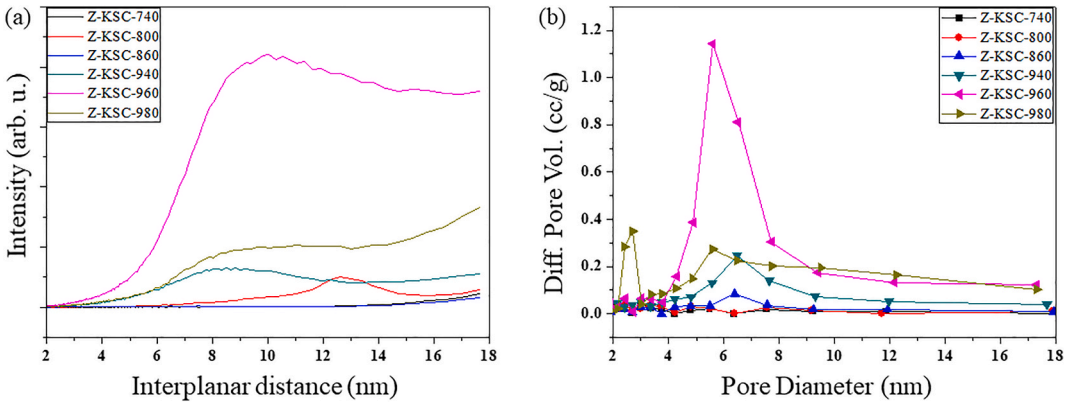


**Fig. 11.** (a) Interplanar distances from low-angle XRD (LA-XRD) and (b) Barrett–Joyner–Halenda (BJH) pore size distributions (PSD) of Z-KSC samples.

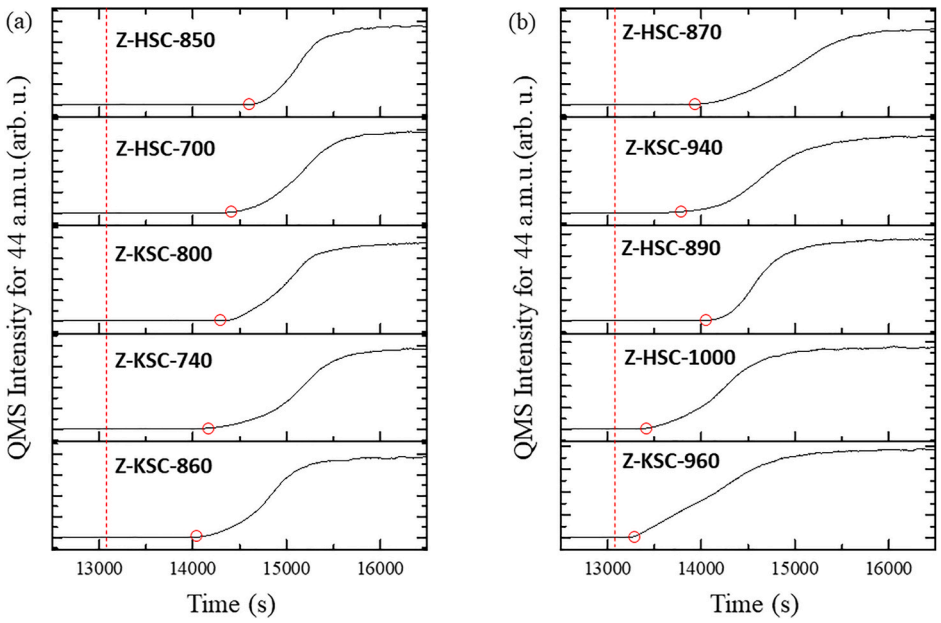


**Fig. 12.** Dynamic $CO_2$ adsorption breakthrough curves of 44 a.m.u signal recorded residual gas analyzer under continuous 20 sccm 2% $CO_2$ gas flow of (a) zeolite 4A samples and (b) 4A + 13X and 13X samples. Red dashed-line vertical to the x axis corresponds to gas switch point from Ar to 2% $CO_2$. Red circles pinned on $CO_2$ curve represents the point where $CO_2$ signal rise up. (For interpretation of the references to colour in this figure legend, the reader is referred to the Web version of this article.)

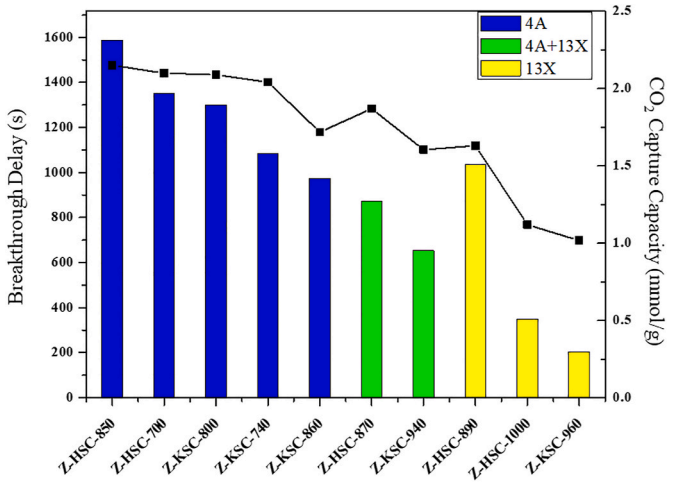


**Fig. 13.** Comparative analysis of $CO_2$ adsorption characteristics in various zeolite samples. Breakthrough delay times (bar chart, left axis) are displayed for zeolite types 4A (blue), 4A + 13X mixtures (green), and 13X with potential mesoporous structures (yellow). The $CO_2$ capture capacity for each sample is depicted by the connected data points (line graph, right axis). (For interpretation of the references to colour in this figure legend, the reader is referred to the Web version of this article.)

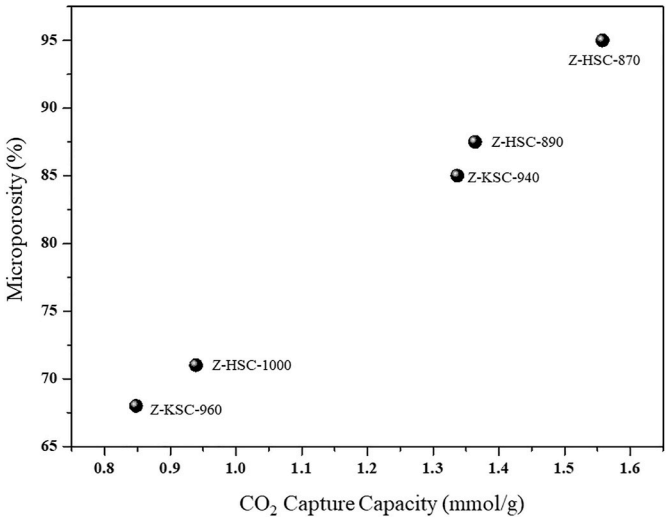


**Fig. 14.** Relationship between $CO_2$ capture capacity (mmol/g) and microporosity (%) for various kaolin and halloysite-based zeolite samples.

microporosity percentage of 87.5%, shows an improved $CO_2$ capture capacity. This aligns with the expectation that more micropores provide more sites for $CO_2$ to adsorb, enhancing the capture efficiency (Fig. 14). Moreover, the presence of a mesoporous spinel structure within these zeolites creates a micro-meso composite, which offers a unique combination of small micropores and larger mesopores. This dual porosity can influence the diffusion dynamics of $CO_2$, potentially enhancing the capture capacity and affecting the breakthrough delay as $CO_2$ molecules have multiple pathways and sites for adsorption.

Fig. 15 presents an intriguing comparison of $CO_2$ adsorption capacities among a series of zeolite samples, with an observable trend related to the composition of the zeolite type, particularly the proportion of zeolite 4A present until micro-meso zeolitic composites of zeolite 13X samples change the interaction between saturation and breakthrough adsorption capacities. Robust saturation adsorption capacities were reflected in the blue bars, and substantial, yet lower, breakthrough capacities in orange were observed in Fig. 15. This pattern is consistent with the known properties of 4A zeolites—high microporosity leads to an extensive capacity for $CO_2$ adsorption, but not all of this capacity is exploited at the breakthrough point. The blend samples, Z-HSC-870 and Z-KSC-940, demonstrate the impact of combining 4A with 13X zeolites. Here, the presence of 13X begins to assert its influence, potentially offering a broader range of pore sizes which contributes to a different adsorption behavior compared to the pure 4A samples. These samples show a high overall saturation capacity but a marked reduction in breakthrough capacity, suggesting a more complex adsorption pathway that extends beyond the initial breakthrough phase. Upon reaching Z-

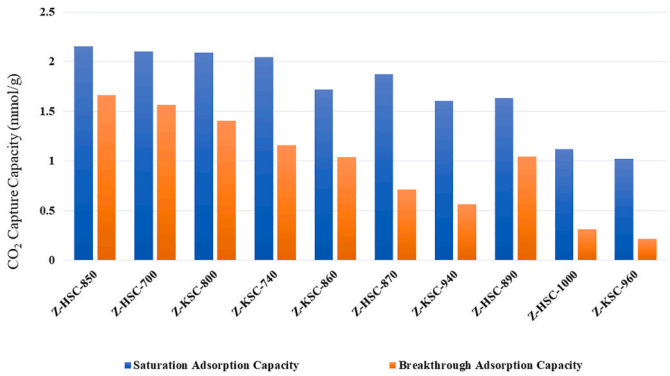


**Fig. 15.** Comparison of saturation and breakthrough adsorption capacities for zeolite samples. The bar graph displays the $CO_2$ adsorption capacities at saturation (blue bars) and at breakthrough (orange bars) for various zeolite samples. (For interpretation of the references to colour in this figure legend, the reader is referred to the Web version of this article.)

HSC-890, where 4A is no longer a component, a significant decline in both saturation and breakthrough capacities was observed. This suggests that while the 13X zeolites and their mesoporous spinel structures contribute positively to the adsorption process, they are less effective than 4A zeolites in terms of overall $CO_2$ capture. The close-ratio between saturation and breakthrough capacities in these samples indicates a more uniform adsorption process, likely due to the mesopores facilitating rapid access and saturation of $CO_2$ within the material.

Fig. 16 provides a summary of the $CO_2$ capture capacities of different sorbent materials across a range of solar calcination temperatures, extending from roughly 700 °C–1000 °C. It distinguishes two categories of sorbent performance, indicated by black (Z-HSC) and red (Z-KSC) lines. Notably, the "no zeolite, GA + Q" sample, exhibits minimal $CO_2$ capture capability, underscoring the pivotal role of zeolites in the adsorption process. As the calcination temperature of the clays increases, the zeolite type changes from 4A to 13X, and $CO_2$ capture performances decrease. The graph effectively illustrates how different sorbent materials are affected by temperature in the context of $CO_2$ capture, which is vital for the optimization of these materials for $CO_2$ capture applications.

The performance of our zeolites was contextualized within the existing literature in Table 2, revealing both consistencies and variances that call attention to the complex interplay between zeolite type, synthesis conditions, and clay mineralogy in determining $CO_2$ uptake efficiency. Our findings indicate that the $CO_2$ capture capacity of 4A zeolites synthesized in this work aligns closely with the capacities of 4A zeolites reported in the literature, suggesting that our synthesis approach yields materials with competitive adsorption properties. However, there remains a slight deviation when compared to commercial 4A zeolites, potentially attributed to differences in porosity, surface area, impurities, and the presence of active sites essential for $CO_2$ adsorption.

The performance of 13X zeolites synthesized from the minerals demonstrated a broader range of $CO_2$ uptake capacities, aligning with the variability observed in the literature. The variability underlines the sensitivity of 13X zeolites to the specific details of synthesis and post-synthesis treatments, suggesting that optimization in these areas could

**Table 2**
$CO_2$ capture capacity of zeolite 4A and 13X at 25 °C and 1 bar.

| Clay Mineral | Zeolite Type | $CO_2$ Uptake (mmol/g) | Ref. |
|---|---|---|---|
| Kaolinite | 13X | 2 | (Garshasbi et al., 2017) |
| Feldspar | 13X | 1 | (Garshasbi et al., 2017) |
| Bentonite | 13X | 1 | (Garshasbi et al., 2017) |
| Bentonite | 13X | 4.79 | (Chen et al, 2014) |
| Kaolinite | 13X | 2.09 | Jia et al. (2024) |
| – | Commercial 4A | 3.64 | Chen and Ahn (2014) |
| – | Meso 4A | 2.95 | Chen and Ahn (2014) |
| – | Commercial 13X | 3.36 | Sun et al. (2024) |
| Kaolinite | 4A | 2.4 | Cecilia et al. (2022) |
| Halloysite | 13X | 4.3 | Lu et al. (2022) |
| Basalt Rock | 4A | 1.9 | Hwang et al. (2018) |
| Kaolinite | 4A | 2.09 | This work |
| Kaolinite | 13X | 1.02 | This work |
| Halloysite | 4A | 2.15 | This work |
| Halloysite | 13X | 1.64 | This work |

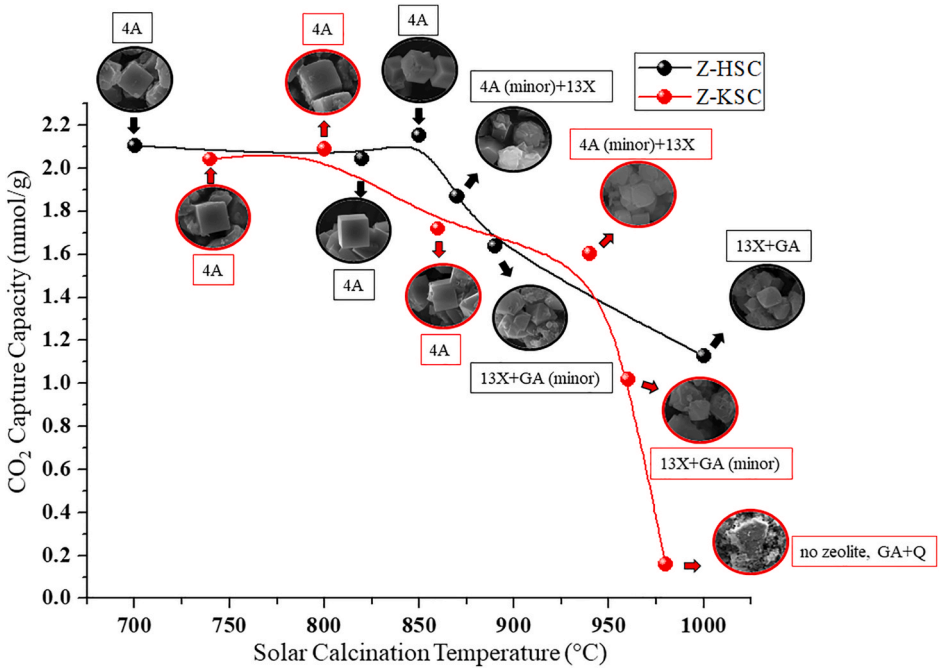


**Fig. 16.** The influence of solar calcination temperature on the synthesized zeolite type and $CO_2$ capture capacity.

lead to significant improvements in $CO_2$ capture performance. It must be clearly stated that all 13X samples except ours given in Table 2 had gone through alterations to make the precursor clay suitable for 13X syntheses, such as acid treatments, the addition of high-grade commercial silica, alkali fusion, and organic templates. Notably, the lower $CO_2$ uptake observed in our 13X samples compared to the highest values reported in the literature points towards the potential for further enhancement through post-synthesis modifications such as ion exchange and surface modifications. Replacing the cations (e.g., $Na^+$ in 4A and 13X) with other cations such as $Ca^{2+}$, $Li^+$, or $Mg^{2+}$ can enhance $CO_2$ adsorption by increasing the electrostatic interaction between $CO_2$ molecules and the zeolite framework (Chen et al., 2017; Boer et al., 2023; Shrotri et al., 2024). Amine modification of zeolites has gained attention as a promising approach for $CO_2$ adsorption at low pressures (Panda et al., 2019). The synergistic interaction between amine groups and $CO_2$, along with the use of mesoporosity-inducing templates, makes zeolites highly effective materials for carbon dioxide capture (Boer et al., 2022).

The reversibility of $CO_2$ capture is crucial for practical applications of sorbent materials. The highest $CO_2$ capture sample Z-HSC-850, saturated with $CO_2$, was investigated for regeneration using high-flow Argon flush and temperature-programmed desorption (TPD) experiments. Initially, $CO_2$ adsorption was followed by a high-flow (200 ml/min) Argon flush to remove weakly adsorbed $CO_2$ species from the material's surface and internal cages. SI-3a shows the delay observed when switching from a 20 ml/min $CO_2$ flow to a 200 ml/min Argon flow, with the shaded area indicating that approximately 96% of the captured $CO_2$ was removed during the flush. For complete regeneration, the sample was heated to 750 °C to remove chemically bound $CO_2$ species such as monodentate and bidentate carbonates. The TPD profile (SI-3b) revealed two primary desorption peaks at 160 °C and 280 °C, confirming the effective removal of the remaining $CO_2$. This demonstrates that $CO_2$ storage in Z-HSC-850 is highly reversible under ambient conditions, with the majority (~96%) desorbed at room temperature using an Argon flush. The small fraction of $CO_2$ requiring higher temperatures (up to 280 °C) for desorption indicates that the material can be regenerated with relatively low energy input, enhancing its commercial viability for sustainable $CO_2$ capture and storage applications.

This work highlights the promising potential of solar-driven zeolite synthesis from clays, which, with targeted advancements mentioned above, could not only compete with but also surpass market-available alternatives. Such an approach lays the foundation for an industry focused on "green" zeolites, starting a new era of sustainable and eco-friendly solutions.

## 4. Conclusion

In this study, we have systematically investigated the $CO_2$ capture capacities of 4A and 13X zeolites synthesized using various clay minerals kaolin, and halloysite. By using a solar simulator, we have successfully synthesized zeolites 4A and 13X, exhibiting outstanding $CO_2$ adsorption capacities, notably for zeolite 4A which presented an adsorption capacity of 2.15 mmol/g at 25 °C and 1 bar pressure. Through extensive characterization and $CO_2$ capture studies, we have also highlighted the role of Al-Si spinel within the zeolite 13X matrix in creating a secondary mesoporous phase, which, while interesting, showed minimal influence on the breakthrough adsorption $CO_2$ capture performance. Furthermore, our work has established LA-XRD as a potent alternative method for the assessment of mesoporosity in zeolitic materials, paving the way for future research and practical applications. This research underlines the importance of temperature control during the calcination process, which has been shown to critically affect the type of zeolite synthesized and their subsequent $CO_2$ capture capacities. By harnessing solar energy for calcination, we have not only mitigated the environmental impact of zeolite synthesis from clays but also used these solar-produced zeolites for $CO_2$ capture. The findings of this study reinforce the promising nature of solar-driven processes for producing zeolites from halloysite and kaolin, which, with further optimization, could lead to the creation of advanced materials for environmental remediation and greenhouse gas reduction. It opens new horizons for the synthesis of "green" zeolites and sets a precedent for sustainable practices in material science and engineering, highlighting the potential of solar energy in addressing critical environmental challenges.

## CRediT authorship contribution statement

**Pelin Pasabeyoglu:** Writing – original draft, Visualization, Validation, Resources, Methodology, Investigation, Formal analysis, Data curation, Conceptualization. **Erdem Deniz:** Methodology, Investigation, Formal analysis. **Gkiokchan Moumin:** Validation, Investigation, Formal analysis. **Zafer Say:** Writing – original draft, Visualization, Validation, Supervision, Project administration, Investigation, Formal analysis, Data curation. **Burcu Akata:** Writing – original draft, Supervision, Resources, Project administration, Funding acquisition.

## Declaration of competing interest

The authors declare that they have no known competing financial interests or personal relationships that could have appeared to influence the work reported in this paper.

## Data availability

Data will be made available on request.

## Acknowledgements

The European Union's Horizon 2020 Research and Innovation programme, under grant agreement no. 856619, has funded this project. We gratefully acknowledge the support provided by METU-Central Laboratory.

## Appendix A. Supplementary data

Supplementary data to this article can be found online at https://doi.org/10.1016/j.jclepro.2024.143838.

## References

Bakera, A.T., Alexander, M.G., 2019. Use of metakaolin as a supplementary cementitious material in concrete, with a focus on durability properties. RILEM Technical Letters 4, 89–102. https://doi.org/10.21809/rilemtechlett.2019.94.

Baldovino-Medrano, V.G., Niño-Celis, V., Isaacs Giraldo, R., 2023. Systematic analysis of the nitrogen adsorption-desorption isotherms recorded for a series of materials based on microporous-mesoporous amorphous aluminosilicates using classical methods. J. Chem. Eng. Data 68 (9), 2512–2528. https://doi.org/10.1021/acs.jced.3c00257.

Bao, Lixia, Peifeng Gao, S.P., 2020. Analysis method of pore size distribution of porous materials. Mater. Sci. 10 (2), 95–103. https://doi.org/10.12677/ms.2020.102012.

Belviso, C., et al., 2013. A and X-type zeolites synthesised from kaolinite at low temperature. Appl. Clay Sci. 80–81, 162–168. https://doi.org/10.1016/j.clay.2013.02.003.

Boer, D.G., et al., 2022. Binderless zeolite LTA beads with hierarchical porosity for selective CO2 adsorption in biogas upgrading. Microporous Mesoporous Mater. 344 (August), 112208. https://doi.org/10.1016/j.micromeso.2022.112208.

Boer, D.G., Langerak, J., Pescarmona, P.P., 2023. Zeolites as selective adsorbents for CO2 separation. ACS Appl. Energy Mater. 6 (5), 2634–2656. https://doi.org/10.1021/acsaem.2c03605.

Bundy, W.M., 1993. The diverse industrial applications of kaolin. In: Murray, H.H., Bundy, W.M., Harvey, C.C. (Eds.), Kaolin Genesis and Utilization. Clay Minerals Society. https://doi.org/10.1346/CMS-SP-1.3, 0.

Buyondo, K.A., Kasedde, H., Kirabira, J.B., 2022. A comprehensive review on kaolin as pigment for paint and coating: recent trends of chemical-based paints, their environmental impacts and regulation. Case Studies in Chem. Environ. Eng. 6 (August), 100244. https://doi.org/10.1016/j.cscee.2022.100244.

Cecilia, J.A., et al., 2022. Kaolinite-based zeolites synthesis and their application in CO2 capture processes. Fuel 320 (March). https://doi.org/10.1016/j.fuel.2022.123953.

Chakraborty, A., Das, S., Gupta, S., 2003. Evidence for two stage mullite formation during thermal decomposition of kaolinite. Br. Ceram. Trans. 102 (4), 153–157. https://doi.org/10.1179/096797803225004972.

Chauffeton, C., Wallez, G., 2022. Crystal-chemical investigation of the “cubic Al–Si spinel” issued from the thermal transformation of kaolinite and halloysite. J. Am. Ceram. Soc. 105 (7), 4986–4993. https://doi.org/10.1111/jace.18439.
Chen, C., Ahn, W.S., 2014. CO 2 adsorption on LTA zeolites: effect of mesoporosity. Appl. Surf. Sci. 311, 107–109. https://doi.org/10.1016/j.apsusc.2014.04.218.
Chen, C., Park, D.W., Ahn, W.S., 2014. CO 2 capture using zeolite 13X prepared from bentonite. Appl. Surf. Sci. 292, 63–67. https://doi.org/10.1016/j.apsusc.2013.11.064.
Chen, S.J., et al., 2017. Using 13X, LiX, and LiPdAgX zeolites for CO2 capture from post-combustion flue gas. Appl. Energy 191, 87–98. https://doi.org/10.1016/j.apenergy.2017.01.031.
Cho, K., et al., 2009. Generation of mesoporosity in LTA zeolites by organosilane surfactant for rapid molecular transport in catalytic application. Chem. Mater. 21 (23), 5664–5673. https://doi.org/10.1021/cm902861y.
Fenelonov, V.B., Romannikov, V.N., Derevyankin, A.Y., 1999. Mesopore size and surface area calculations for hexagonal mesophases (types MCM-41, FSM-16, etc.) using low-angle XRD and adsorption data. Microporous Mesoporous Mater. 28 (1), 57–72. https://doi.org/10.1016/S1387-1811(98)00280-7.
Feng, Y.C., et al., 2013. Synthesis of mesoporous LTA zeolites with large BET areas. J. Porous Mater. 20 (3), 465–471. https://doi.org/10.1007/s10934-012-9617-7.
Garshasbi, V., Jahangiri, M., Anbia, M., 2017. Equilibrium CO 2 adsorption on zeolite 13X prepared from natural clays. Appl. Surf. Sci. 393, 225–233. https://doi.org/10.1016/j.apsusc.2016.09.161.
Groen, J.C., et al., 2004. On the introduction of intracrystalline mesoporosity in zeolites upon desilication in alkaline medium. Microporous Mesoporous Mater. 69 (1–2), 29–34. https://doi.org/10.1016/j.micromeso.2004.01.002.
Hartmann, M., Thommes, M., Schwieger, W., 2021. Hierarchically-Ordered zeolites: a critical assessment. Adv. Mater. Interfac. 8 (4). https://doi.org/10.1002/admi.202001841.
Hwang, K.J., et al., 2018. Synthesis of zeolitic material from basalt rock and its adsorption properties for carbon dioxide. RSC Adv. 8 (17), 9524–9529. https://doi.org/10.1039/c8ra00788h.
Indira, V., Abhitha, K., 2022. A review on recent developments in Zeolite A synthesis for improved carbon dioxide capture: implications for the water-energy nexus. Energy Nexus 7 (June), 100095. https://doi.org/10.1016/j.nexus.2022.100095.
Ishii, Y., et al., 2013. Pore size determination in ordered mesoporous materials using powder X-ray diffraction. J. Phys. Chem. C 117 (35), 18120–18130. https://doi.org/10.1021/jp4057362.
Jia, W., et al., 2024. Characterization and application of lamellar zeolite-X prepared from kaolin. Micro & Nano Lett. 19 (1), 2–11. https://doi.org/10.1049/mna2.12182.
Kirdeciler, S.K., Akata, B., 2020. One pot fusion route for the synthesis of zeolite 4A using kaolin. Adv. Powder Technol. 31 (10), 4336–4343. https://doi.org/10.1016/j.apt.2020.09.012.
Kumar, S., Srivastava, R., Koh, J., 2020. Utilization of zeolites as CO2capturing agents: advances and future perspectives. J. CO2 Util. 41 (April), 101251. https://doi.org/10.1016/j.jcou.2020.101251.
Li, W., et al., 2015. Facile control of inter-crystalline porosity in the synthesis of size-controlled mesoporous MFI zeolites via in situ conversion of silica gel into zeolite nanocrystals for catalytic cracking. CrystEngComm 17 (30), 5680–5689. https://doi.org/10.1039/c5ce00637f.
Lu, X., et al., 2022. Zeolite-X synthesized from halloysite nanotubes and its application in CO2 capture. J. Taiwan Inst. Chem. Eng. 133, 104281. https://doi.org/10.1016/j.jtice.2022.104281.
Martínez, T.L.M., et al., 2019. Synthesis and identification methods for zeolites and MOFs. Zeolites and Metal-Organic Frameworks 25–52. https://doi.org/10.2307/j.ctvcmxprm.5.
Maschmeyer, T., van de Water, L., 2006. An overview of zeolite, zeotype and mesoporous solids chemistry: design, synthesis and catalytic properties, microporous and mesoporous solid catalysts. https://doi.org/10.1002/0470094214.ch1.
Novembre, D., et al., 2011. Synthesis and characterization of Na-X, Na-A and Na-P zeolites and hydroxysodalite from metakaolinite. Clay Miner. 46 (3), 339–354. https://doi.org/10.1180/claymin.2011.046.3.339.
Ojeda, M.L., et al., 2003. On comparing BJH and NLDFT pore-size distributions determined from N2 sorption on SBA-15 substrata. Phys. Chem. Chem. Phys. 5 (9), 1859–1866. https://doi.org/10.1039/b300821e.
Palomino, M., et al., 2010. New insights on C02-methane separation using LTA zeolites with different Si/Al ratios and a first comparison with MOFs. Langmuir 26 (3), 1910–1917. https://doi.org/10.1021/la9026656.
Panda, D., Kumar, E.A., Singh, S.K., 2019. Amine modification of binder-containing zeolite 4A bodies for post-combustion CO2 capture. Ind. Eng. Chem. Res. 58 (13), 5301–5313. https://doi.org/10.1021/acs.iecr.8b03958.
Panda, D., Kumar, E.A., Singh, S.K., 2020. Introducing mesoporosity in zeolite 4A bodies for Rapid CO2capture. J. CO2 Util. 40 (June), 101223. https://doi.org/10.1016/j.jcou.2020.101223.
Pasabeyoglu, P., et al., 2023. Solarization of the zeolite production: calcination of kaolin as proof-of-concept. J. Clean. Prod. 414 (March), 137611. https://doi.org/10.1016/j.jclepro.2023.137611.
Pérez-Ramírez, J., et al., 2008. Hierarchical zeolites: enhanced utilisation of microporous crystals in catalysis by advances in materials design. Chem. Soc. Rev. 37 (11), 2530–2542. https://doi.org/10.1039/b809030k.
Ptáček, P., et al., 2010. The kinetics of Al-Si spinel phase crystallization from calcined kaolin. J. Solid State Chem. 183 (11), 2565–2569. https://doi.org/10.1016/j.jssc.2010.08.030.
Ptáček, P., et al., 2013. Crystallization of spinel phase from metakaoline: the nonisothermal thermodilatometric CRH study. Powder Technol. 243, 40–45. https://doi.org/10.1016/j.powtec.2013.03.031.
Qoniah, I., et al., 2015. Direct synthesis of mesoporous aluminosilicates from Indonesian kaolin clay without calcination. Appl. Clay Sci. 118, 290–294. https://doi.org/10.1016/j.clay.2015.10.007.
Sachse, A., et al., 2017. Development of intracrystalline mesoporosity in zeolites through surfactant-templating. Cryst. Growth Des. 17 (8), 4289–4305. https://doi.org/10.1021/acs.cgd.7b00619.
Sanz-Pérez, E.S., et al., 2016. Direct capture of CO2 from ambient air. Chem. Rev. 116 (19), 11840–11876. https://doi.org/10.1021/acs.chemrev.6b00173.
Shrotri, A.R., et al., 2024. Performance of Li exchange hierarchical X zeolite for CO2 adsorption and H2 separation. J. Ind. Eng. Chem. 133 (November 2023), 505–514. https://doi.org/10.1016/j.jiec.2023.12.027.
Singh, B.K., et al., 2021. Synthesis of mesoporous zeolites and their opportunities in heterogeneous catalysis. Catalysts 11 (12). https://doi.org/10.3390/catal11121541.
Sun, X., et al., 2024. Maximizing the utilization of Calcium species in the supercages of CaNa-FAU zeolite for efficient CO2 capture. Chem. Eng. J. 481 (November 2023), 148661. https://doi.org/10.1016/j.cej.2024.148661.
Thommes, M., et al., 2015. Physisorption of gases, with special reference to the evaluation of surface area and pore size distribution (IUPAC Technical Report). Pure Appl. Chem. 87 (9–10), 1051–1069. https://doi.org/10.1515/pac-2014-1117.
Urbonavicius, M., et al., 2020. Production of gamma alumina using plasma-treated aluminum and water reaction byproducts. Materials 13 (6), 1–12. https://doi.org/10.3390/ma13061300.
Vu, X.H., Armbruster, U., Martin, A., 2016. Micro/mesoporous zeolitic composites: recent developments in synthesis and catalytic applications. Catalysts 6 (12). https://doi.org/10.3390/catal6120183.
Xue, Z., et al., 2012. Hierarchical structure and catalytic properties of a microspherical zeolite with intracrystalline mesopores. Acta Mater. 60 (16), 5712–5722. https://doi.org/10.1016/j.actamat.2012.06.044.
Yassin, F.M., et al., 2021. Low-angle X-ray scattering for the determination of the size of mesoporous silica nanoparticles. Radiat. Phys. Chem. 179, 109235. https://doi.org/10.1016/j.radphyschem.2020.109235. August 2020.
Yuan, P., et al., 2012. Changes in structure, morphology, porosity, and surface activity of mesoporous halloysite nanotubes under heating. Clay Clay Miner. 60 (6), 561–573. https://doi.org/10.1346/CCMN.2012.0600602.
Zhang, B., et al., 2020. Geopolymerization of halloysite via alkali-activation: dependence of microstructures on precalcination. Appl. Clay Sci. 185 (September 2019), 105375. https://doi.org/10.1016/j.clay.2019.105375.
Zhang, Y., et al., 2024. Porous sorbents for direct capture of carbon dioxide from ambient air. Chin. Chem. Lett., 109676 https://doi.org/10.1016/j.cclet.2024.109676.